Manipulation of valley pseudospin in WSe_2/CrI_3 heterostructures by the magnetic proximity effect

Tao Hu,[1] Guodong Zhao,[1] Heng Gao,[1] Yabei Wu,[1] Jisang Hong,[3] Alessandro Stroppa,[2] and Wei Ren[1,*]

[1]*State Key Laboratory of Advanced Special Steel, Shanghai Key Laboratory of High Temperature Superconductors, MGI, ICQMS, and Department of Physics, Shanghai University, Shanghai 200444, China*

[2]*CNR-SPIN c/o Università degli Studi dell'Aquila, Via Vetoio - 67100 - Coppito (L'Aquila), Italy*

[3]*Department of Physics, Pukyong National University, Busan 608–737, Korea*

(Received 19 December 2018; revised manuscript received 31 January 2020; accepted 3 February 2020; published 2 March 2020)

Removing valley degeneracy is a necessary condition for manipulating valley degrees of freedom and storing information in future spintronics. Magnetic proximity effect has been demonstrated to be an effective way to introduce exchange interactions, especially in the case of two-dimensional (2D) van der Waals (vdW) heterostructures. We have explored the electronic properties and the valley physics of 2D WSe_2/CrI_3 using first-principles calculations. Our results show that a valley splitting of 2 meV is achieved in WSe_2/CrI_3 heterostructures thanks to the coexistence of inversion and time-reversal symmetry breaking. This value corresponds to an effective magnetic field of ∼10 T in experiments. Moreover, we demonstrate that the valley splitting is a robust feature regardless of the stacking configuration and the thickness of CrI_3. Most importantly, by reversing the magnetization in the CrI_3 layer, the valley splitting and polarization at K^+ and K^- points are completely switchable. Our findings provide fundamental insights into the magnetoelectric spin-orbit coupling based spintronics applications of 2D vdW heterostructures.

DOI: 10.1103/PhysRevB.101.125401

I. INTRODUCTION

In transition-metal dichalcogenide (TMD) monolayer [1–9], a pair of degenerate but inequivalent valleys in momentum space gives rise to interesting phenomena such as valley-dependent photoluminescence [10,11], valley Hall effect [12,13], and valleytronics [14,15]. The energy valleys at the conduction-band minimum (CBM) and valence-band maximum (VBM) are considered as a novel degree of freedom of electrons with the potential that the valley carriers can be manipulated for information technology devices. To exploit valley degrees of freedom, it is important to introduce a valley polarization. However, although the broken-inversion symmetry of TMD monolayers could separate the paired valleys K^+ and K^- in momentum space, the energy degeneracy is still retained since it is protected by the time-reversal symmetry [16]. A magnetic field could then be applied to break the time-reversal symmetry to achieve the valley polarization for potential spintronic applications.

Theoretical calculations have suggested that magnetic ions doping [17,18] or vacancies [19,20] may introduce magnetic moments in TMD monolayer and eventually remove the valley degeneracy. Further, intrinsic valley polarization has been found in magnetic TMDs monolayer VSe_2 [21,22]. Experimentally, it was demonstrated that a vertical external magnetic field could produce a valley Zeeman splitting [23,24] of about 0.1–0.2 meV/T. A large valley splitting has been reported theoretically in TMD monolayer on EuO [25,26] or EuS [27] substrate. Recently, an enhanced valley spitting in monolayer WSe_2 has been experimentally investigated by exploiting the magnetic proximity effect (MPE) from the EuS substrate [28].

A specific material can obtain novel properties due to the presence of neighboring material, i.e., by the so-called proximity effect. In particular, the MPE means that the host's properties are modified mainly by magnetic neighbors [29–33]. The successful exfoliation discovery of two-dimensional (2D) ferromagnets [34,35] would introduce an unprecedent opportunity, which provides a way of interfacing TMD monolayers with ferromagnetic layers. Indeed, a van der Waals (vdW) heterostructure would minimize chemical modification and interfacial damage [36], which is desirable for engineering a clean interface for optimal interactions [37].

Within this framework, we performed theoretical investigations of the valley pseudospin in WSe_2 monolayer on a 2D magnetic CrI_3 substrate. We explain the mechanism how the valley properties are modified by the MPE, with a significant valley splitting of 2.0 meV, which is also related to the experimental observation [38,39]. Moreover, we demonstrate the valley splitting and polarization performance is robust in the vdW stackings of WSe_2/CrI_3, so that a magnetic field can be applied to achieve the manipulation of the valley degree of freedom. Interestingly, since the MPE is a *localized* surface effect, a bilayer CrI_3 with zero net magnetic moment can also induce a valley splitting and polarization. We believe that this is important because the MPE valley splittings can be achieved by using antiferromagnetic (AFM) materials, thus extending the valley physics to AFM spintronics. This certainly suggests further exploration directions, both from theoretical and experimental points of view.

*renwei@shu.edu.cn

II. COMPUTATIONAL METHODS

The first-principles calculations were performed using the projector-augmented wave approach [40,41] implemented in the Vienna *Ab initio* Simulation Package (VASP) [42,43]. The vdW heterostructures are all constructed with a substrate monolayer of CrI_3 and a capping monolayer of WSe_2, including a vacuum separation larger than 18 Å. The heterostructures with different spin configurations were fully optimized with Perdew-Burke-Ernzerhof (PBE) generalized-gradient approximation (GGA) [44] exchange-correlation functional together with optB86b-vdW functional [45,46], until the force on each atom was below 0.001 eV/Å. Their electronic self-consistent convergence criterion for self-consistent calculations was set to 10^{-7} eV. The plane-wave energy cutoff was set as 600 eV. A $7 \times 7 \times 1$ Γ (0, 0, 0) centered k-point grid was sampled in the first Brillouin zone. Band-structure calculations with or without spin-orbit coupling (SOC) were performed; the k-point path of SOC band-structure calculations was chosen to include $\Gamma - M^+$ (0, 0.5, 0)$-K^+$ $(-1/3, 2/3, 0) - \Gamma - M^-(0.5, 0, 0) - K^-(1/3, 1/3, 0) - \Gamma$.

To further illustrate the valley properties of the WSe_2/CrI_3 heterostructure the out-of-plane Berry curvature $\Omega(k)$ is calculated by the usual linear response Kubo formula [47]

$$\Omega(k) = \sum_n f_n \Omega_n(k), \tag{1}$$

$$\Omega_n(k) = -2Im \sum_{m \neq n} \frac{\langle u_{nk}|v_x|u_{mk}\rangle\langle u_{mk}|v_y|u_{nk}\rangle}{(E_{mk} - E_{nk})^2}, \tag{2}$$

where f_n is the Fermi-Dirac distribution function, $v_{x,y}$ is the velocity operator, and u_{nk} is the periodic part eigenvector with eigenvalue E_{nk} of the Fourier transformed Wannier Hamiltonian as calculated by projecting the density-functional theory (DFT) Hamiltonian onto a Wannier basis. In this case, we used the d orbitals of W and Cr atoms and p orbitals of Se and I atoms to construct the maximally localized Wannier function by the WANNIER90 package [48]. We used a large k mesh of $100 \times 100 \times 1$ to calculate the Berry curvature in the first Brillouin zone.

III. RESULTS AND DISCUSSION

The optimized lattice constants of monolayer CrI_3 and WSe_2 are 6.85 and 3.30 Å, respectively, which are very close to the experimental [49,50] and other theoretical [51,52] results. Our calculations show that the magnetic moment of one CrI_3 unit cell is 6 μ_B corresponding to a Cr magnetic moment of 3.06 μ_B, which is also consistent with a previous study [51]. Despite the presence of localized 3d electronic states on Cr atoms, both GGA and DFT + U approaches reproduce similar results as far as the magnetic properties are concerned [53]. Therefore, in the following, we do not consider the U corrections of 3d states of Cr.

To form a WSe_2/CrI_3 heterostructure, we use a (1×1) primitive cell of monolayer CrI_3 and a (2×2) supercell of monolayer WSe_2. This bilayer contains 20 atoms (2 Cr, 6 I, 4 W, and 8 Se atoms) in total. The in-plane lattice parameter of the heterostructure is fixed to 6.85 Å which is the in-plane lattice constant of the monolayer CrI_3, thus introducing a tensile strain of ~3.8% applied to WSe_2. The atomic structure of the WSe_2/CrI_3 heterostructure is presented in Fig. 1. We considered three different stackings, namely, two high-symmetry configurations: H and T for hollow and top cases as shown in Figs. 1(a) and 1(b), and one low-symmetry R (for random) configuration as shown in Fig. 1(c). The interlayer distance is calculated to be 3.52 Å for H-WSe_2/CrI_3, which is in the range of typical value for vdW heterostructures [54–56]. The other two configurations have comparable interlayer distances, 3.52 and 3.56 Å for T- and R-WSe_2/CrI_3, respectively.

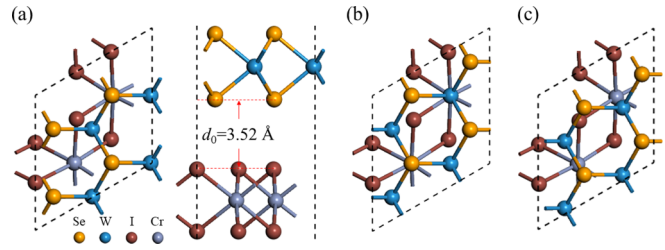

FIG. 1. (a) Top and side views of the hollow WSe_2/CrI_3 (H-WSe_2/CrI_3) vdW heterostructure. In this configuration, one Cr atom is located near the center of WSe_2 hexagon and the other Cr atom is below Se atom. The distance between the CrI_3 and WSe_2 layers is indicated as d_0. (b) Top view of the top WSe_2/CrI_3 (T-WSe_2/CrI_3) heterostructure in which two corners of WSe_2 hexagon are right on the top of Cr atoms. One Cr atom is below Se atom, and the other one is below W atom. (c) Top view of the random WSe_2/CrI_3 (R-WSe_2/CrI_3) heterostructure in which the two layers are randomly stacked without any specific positioning.

We have then calculated the binding energy of the WSe_2/CrI_3 heterostructures using a relation $E_b = E_{CrI_3} + E_{WSe_2} - E_{WSe_2/CrI_3}$, where E_{WSe_2/CrI_3}, E_{CrI_3}, and E_{WSe_2} are defined as the total energies of the heterostructure, isolated monolayer CrI_3, and isolated WSe_2 layer, respectively. The three configurations (H, T, R) have the binding energy (E_b divided by total atom number of CrI_3) of 73, 72, and 71 meV, respectively. These values are comparable to other vdW systems such as graphite [57], bulk hexagonal boron nitride (h-BN) [58], and h-BN/phosphorene heterostructures [54].

Figure 2(a) illustrates the band structure of the bare monolayer WSe_2 at the K^+ (K^-) valley. It has a twofold valley degree of freedom in the Brillouin zone, which is protected by time-reversal symmetry. Due to the broken-inversion symmetry and strong SOC in WSe_2, valley-dependent selection rules must be obeyed in the interband optical transitions, which are allowed only with $\sigma^+(\sigma^-)$ circularly polarized optical field at the $K^+(K^-)$ valley [59]. Moreover, the energies of the circularly polarized lights are equivalent to each other ($E_{\sigma^+} = E_{\sigma^-}$). In the presence of magnetic field **B** perpendicular to the interface, as shown in Fig. 2(b), valley degeneracy is lifted by the magnetic field. Now, the nonequivalent K valleys can not only be distinguished by the valley and spin indices, but also by the energy ($E_{\sigma^+} \neq E_{\sigma^-}$).

Figure 2(c) presents the band structure (PBE + SOC) of freestanding monolayer WSe_2 under a biaxial tensile strain of 3.8%. It clearly shows the typical features at the two degenerate K valleys. The energy corresponding to the σ^+ circularly polarized light in Fig. 2(a) is calculated to be 0.933 eV, while

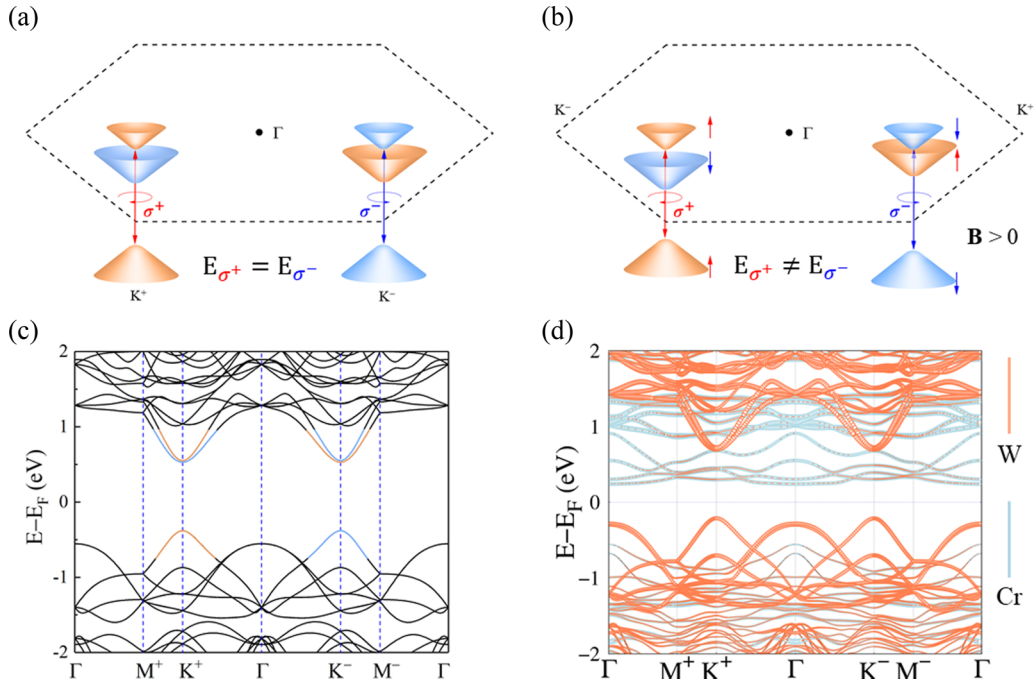

FIG. 2. (a) A schematic diagram of the energy band structure showing the valley-dependent optical selection rule in monolayer TMDs. (b) A schematic diagram showing electronic structures at the K^+ and K^- valleys in the exchange-coupled WSe_2/CrI_3 heterostructure due to magnetic proximity effect. **B** indicates the effective magnetic field induced by CrI_3. (c) Calculated band structure of 2×2 supercell of monolayer WSe_2 with SOC under a biaxial tensile strain of 3.8%. (d) Projected band structure of the WSe_2/CrI_3 heterostructure, where orange and blue curves are of Cr and W atoms.

σ^- circularly polarized light has exactly the same energy. Figure 2(d) presents the orbital projected band structure of the H-WSe_2/CrI_3 heterostructure. The global band gap of the heterostructure is 0.435 eV, while the band gaps of bare CrI_3 and WSe_2 are 0.752 and 0.911 eV, respectively. The calculated orbital projected band structure shows the band alignment of the WSe_2/CrI_3 bilayer, which demonstrates that it is a type-II heterostructure [60]. We see that the orbital hybridization of CrI_3 and WSe_2 is very weak from -1 to 1 eV. The W atoms projected bands near CBM and VBM are almost the same as that of bare WSe_2, which indicates both K^+ and K^- valleys of monolayer WSe_2 are well preserved for CBM and VBM.

The physical binding of monolayer WSe_2 to CrI_3 does not influence its magnetic property. In fact, we observe that the CrI_3 layer in the heterostructure preserves the ferromagnetism with 3.06 μ_B on each Cr atom, which is equivalent to its states in bare CrI_3. After the validation of magnetism of CrI_3, we carefully examine the potential valley Zeeman effect in WSe_2 induced by the MPE from CrI_3. The valley splitting energy (ΔE_σ) is defined by $\Delta E_\sigma = E_{\sigma^+} - E_{\sigma^-}$ as shown by the red and blue double-headed arrows in Figs. 2(a) and 2(b). Interestingly, we obtain $\Delta E_\sigma = -0.5$ meV of valley polarization for the H-WSe_2/CrI_3. It is found that the valley polarization energies are -2.0 and -1.4 meV for the T- and R-WSe_2/CrI_3, which correspond to effective magnetic fields of about 10 and 7 T, respectively, according to the value of 0.1–0.2 meV/T reported in a few experiments [23,61,62]. The T-WSe_2/CrI_3 has a relatively large polarization energy, which is ascribed to one W superimposed on one Cr atom. The relationship between the stacking patterns and the valley polarization energy was well explained in a recent work [63]. Such lifted valley degeneracy persists in different configurations, showing that the magnetic proximity-induced valley polarization is a robust property. The results even suggest that stacking patterns could determine the magnitude of valley Zeeman effect, which provides us a way to manipulate the valley pseudospin. We have also investigated how the in-plane lattice constants of heterostructure affect the valley polarization. More details can be found in the Supplemental Material [64].

Finally, we consider whether the reversal of CrI_3 magnetization affects the valley pseudospin. This is certainly interesting for applications, since it can be achieved by applying an external magnetic field in experiments. The energy cost of the magnetization reversal is not expected to be large, because the magnetic anisotropy energy of CrI_3 monolayer is around 0.69 meV per Cr atom [51]. The same calculations and analysis have been carried out for the three configurations. The results are summarized in Table I. As one can clearly see, ΔE_σ values have the same magnitude, but with opposite signs. Thus, the valley polarization can indeed be switched simply by reversal of the CrI_3 magnetization.

Moreover, when the magnetization of CrI_3 is aligned in plane ($\mathbf{M} \perp z$), the valleys are found to become energetically degenerate again. In other words, only an effective perpendicular magnetic field can produce valley polarization. We can interpret this by the following intuitive picture. Considering the magnetic flux as the surface integral of the normal component of the magnetic field, for a unit vector area **S** of the WSe_2 surface we have

$$\Phi_B = \mathbf{B} \cdot \mathbf{S} = BS\cos\theta, \tag{3}$$

TABLE I. Calculated band gaps and valley splitting energy (ΔE_σ) of the three configurations of WSe_2/CrI_3 heterostructures with two opposite magnetization directions, namely **M**//z (the magnetization points to WSe_2 from substrate CrI_3) and the flipped case **M**// $-z$.

		M//z		**M**// $-z$		**M** $\perp z$
vdW bilayer	Stacking pattern	Band gap (eV)	$E_{\sigma+} - E_{\sigma-}$ (meV)	Band gap (eV)	$E_{\sigma+} - E_{\sigma-}$ (meV)	$E_{\sigma+} - E_{\sigma-}$ (meV)
WSe_2/CrI_3	Hollow (H)	0.435	−0.5	0.437	0.5	0
	Top (T)	0.451	−2.0	0.454	2.0	0
	Random (R)	0.486	−1.4	0.486	1.4	0

where B is the magnitude of the magnetic field from MPE of CrI_3, S is the unit area of CrI_3, and θ is the angle between the magnetic-field vector and the normal to **S**. Therefore, the valley splitting energy with rotation of the magnetization of CrI_3 is

$$\Delta E_\sigma^\theta = \Delta E_\sigma^0 \cos\theta \,, \tag{4}$$

where ΔE_σ^0 is the splitting energy when the magnetic field is perpendicular to the WSe_2 plane ($\theta = 0$). If the magnetization of the CrI_3 is vertically flipped ($\theta = \pi$), then the valley polarization is switched as the values shown in Table I. Our calculations of constrained direction of the Cr magnetic moments also demonstrate the validation of Eq. (4). If we manipulate the magnetization of the substrate CrI_3 from out of plane to in plane, the value of θ changes from 0 to 90°, the valley splitting energy (ΔE_σ) follows cosine function as shown in Fig. 3(a).

In experiments, researchers can change the magnitude of an external magnetic field in order to manipulate the valley degrees of freedom [23,24]. We simulate this effect by changing the interlayer distance of WSe_2/CrI_3 heterostructure. It is expected that the MPE-induced valley splitting could be modulated by the interlayer distance of the heterostructures. Figure 3(b) presents the valley splitting energy (ΔE_σ) of T-WSe_2/CrI_3 as a function of deviation from equilibrium separation. The red dashed curve is fitted to the following exponential function (fitting parameters are presented in section S5 of Supplemental Material [64]):

$$\Delta E_\sigma = 1.93 e^{-(\Delta d/0.34)}, \tag{5}$$

where e is the natural constant, Δd is interlayer distance deviated from the relaxed state. It clearly shows that the valley splitting is very sensitive to the interlayer distance. When the interlayer separation decreases by 0.3 Å, the valley splitting energy is 4.5 meV, which is more than two times of the value of its equilibrium state. While the separation is increased, the splitting energy becomes smaller and smaller; eventually the valley degeneracy almost recovers with a displacement of 1 Å from the equilibrium separation distance.

We have also examined whether the valley polarization disappears if the WSe_2 is placed on the top of bilayer CrI_3 which has an AFM ground state. In Fig. 4 the T-WSe_2/CrI_3 is placed on top of another CrI_3 monolayer. Interestingly, the valley splitting energy is calculated to be 1.9 meV, which is very close to that of bilayer T-WSe_2/CrI_3. One might have expected that the second CrI_3 layer should suppress the valley polarization of T-WSe_2/CrI_3. However, this effect is very weak due to a larger interlayer distance of 10.1 Å between WSe_2 and the second CrI_3 layer. This confirms that the MPE is mainly dominated by the most adjacent CrI_3 layer. The same conclusion has also been drawn by examining layer- and spin-resolved density of states in a recent work [65]. Therefore, it suggests that experimentalists may use both FM and AFM CrI_3 layers to induce the valley polarization. In other words, the valley splitting appears as long as the WSe_2

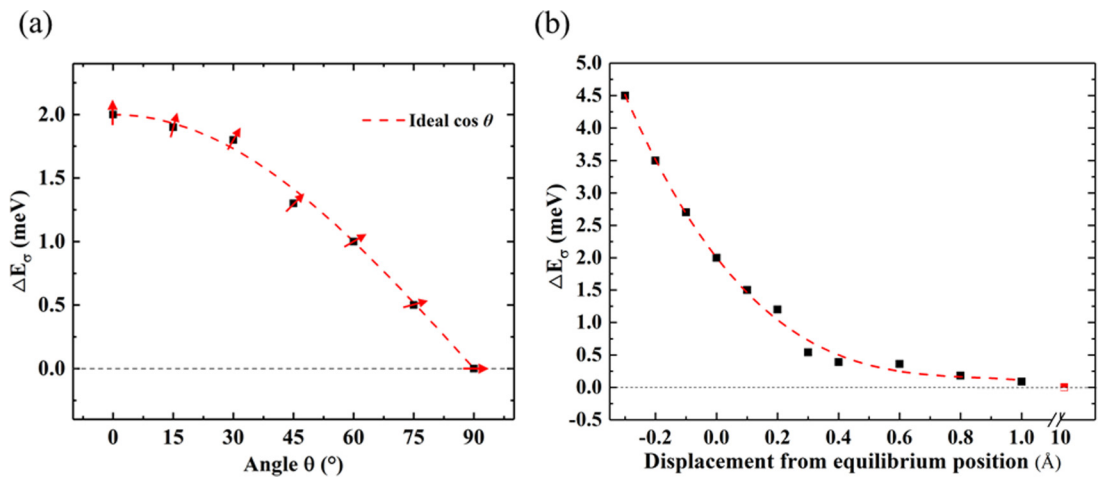

FIG. 3. Calculated valley splitting energy (ΔE_σ) of T-WSe_2/CrI_3 as a function of (a) the magnetization direction of the CrI_3 and (b) the interlayer distance deviation from the position of equilibrium state. The red dashed line in panel (b) is a guide for eyes. The red semifilled square is an extrapolated value.

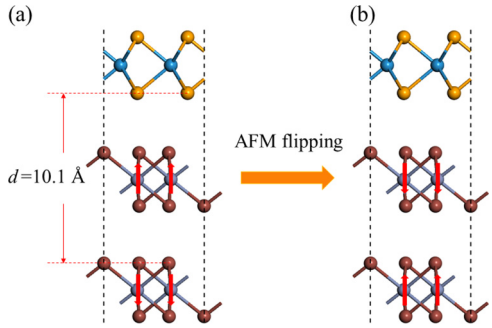

FIG. 4. Schematic illustration of the calculated configurations of T-WSe_2/Bilayer-CrI_3 vdW heterostructure with reversed AFM states.

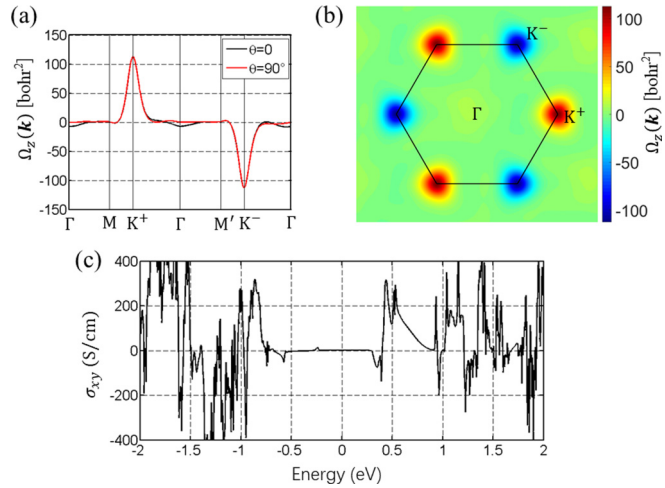

FIG. 5. The out-of-plane Berry curvature $\Omega(k)$ of T-WSe_2/CrI_3 heterostructure (a) along the high-symmetry lines, the black and red curves are calculated with out-of-plane and in-plane magnetizations of CrI_3, and (b) projected in the first Brillouin zone. (c) Anomalous Hall conductivity as a function of the Fermi level in the same energy range as the band structure.

monolayer is placed on the top of CrI_3 layers, no matter if the number of CrI_3 layers is odd or even [64]. This also implies that one can have a complete switching of the MPE valley splitting by switching the AFM order parameter as shown in Fig. 4. However, a hypothetic intralayer AFM-coupled CrI_3 monolayer cannot induce the valley polarization; see Ref. [64].

The proposed WSe_2/CrI_3 heterostructure here definitely breaks the inversion symmetry that is same as freestanding WSe_2. Therefore, we should expect the nonvanishing Berry curvature, as shown in Fig. 5. We find that the calculated out-of-plane Berry curvature $\Omega(k)$ has two peaks at K^+ and K^- with opposite signs due to the presence of inversion symmetry breaking, which is in line with the valley-contrasting Berry curvature in bare TMDs [6]. The Berry curvature has also been calculated in the case of artificially constrained in-plane magnetism CrI_3. It is not significantly changed by the rotation of magnetization direction. We only see tiny difference at the Γ point. In the first Brillouin zone, the C_3-symmetrized $\Omega(k)$ is nonzero only in the vicinity of the valleys as shown in Fig. 5(b). The maximal value of out-of-plane Berry curvature at K points is 120 bohrs^2, which is much larger than the values of 9 bohrs^2 in hydrofluorinated bismuth nanosheet [66] and 58 bohrs^2 in WS_2/MnO heterostructure [67]. When we are integrating the Berry curvature $\Omega(k)$ around K^+ and K^- and then sum them, we obtain a nonzero Berry curvature corresponding to an anomalous Hall effect due to the coexistence of SOC and magnetism. Figure 5(c) shows the calculated anomalous Hall conductivity as a function of the Fermi level. To obtain a fully spin- and valley-polarized Hall conductivity, the Fermi level must lie between the VBM-K^+ and the VBM-K^-.

IV. CONCLUSIONS

In summary, we have studied the MPE-induced valley degeneracy breaking in 2D WSe_2/CrI_3 heterostructures which is more efficient than applying an external magnetic field. The MPE is shown to be a localized effect, which requires no specific interlayer stacking for an excellent platform to realize exchange interaction effects. We found that the valley polarization and splitting energy could be modulated by the interlayer distance engineering and/or the orientation of the substrate magnetic ordering. Moreover, for AFM CrI_3 bilayer substrate with zero net magnetization, MPE can also induce the studied valley splitting. This makes our MPE thickness independent, and it may be further explored in the field of spin-orbitronics as well as AFM spintronics.

ACKNOWLEDGMENTS

This work was supported by the National Natural Science Foundation of China (Grants No. 11804216, No. 51672171, No. 51861145315, and No. 51911530124), the National Key Basic Research Program of China (Grant No. 2015CB921600), Independent Research Project of State Key Laboratory of Advanced Special Steel and Shanghai Key Laboratory of Advanced Ferrometallurgy at Shanghai University, the fund of the State Key Laboratory of Solidification Processing in NWPU (No. SKLSP201703), and the Young Scientists exchange program supported by Ministry of Science and Technology of China and National Research Foundation of Korea. The supercomputing services from AM-HPC, the Chinese Scholarship Council, China Postdoctoral Science Foundation and the Fok Ying Tung Education Foundation are also acknowledged.

[1] S. Manzeli, D. Ovchinnikov, D. Pasquier, O. V. Yazyev, and A. Kis, Nat. Rev. Mater. **2**, 17033 (2017).
[2] T. Mueller and E. Malic, Npj 2D Mater. Appl. **2**, 29 (2018).
[3] H. Yuan, M. S. Bahramy, K. Morimoto, S. Wu, K. Nomura, B.-J. Yang, H. Shimotani, R. Suzuki, M. Toh, C. Kloc, X. Xu, R. Arita, N. Nagaosa, and Y. Iwasa, Nat. Phys. **9**, 563 (2013).

[4] M. Chhowalla, H. S. Shin, G. Eda, L.-J. Li, K. P. Loh, and H. Zhang, Nat. Chem. **5**, 263 (2013).

[5] F. Liu, J. Zhou, C. Zhu, and Z. Liu, Adv. Funct. Mater. **27**, 1602404 (2017).

[6] W. Feng, Y. Yao, W. Zhu, J. Zhou, W. Yao, and D. Xiao, Phys. Rev. B **86**, 165108 (2012).

[7] W. Zhou, J. Chen, H. Gao, T. Hu, S. Ruan, A. Stroppa, and W. Ren, Adv. Mater. **31**, 1804629 (2019).

[8] T. Hu, F. Jia, G. Zhao, J. Wu, A. Stroppa, and W. Ren, Phys. Rev. B **97**, 235404 (2018).

[9] X. Sui, T. Hu, J. Wang, B.-L. Gu, W. Duan, and M.-s. Miao, Phys. Rev. B **96**, 041410(R) (2017).

[10] H. Zeng, J. Dai, W. Yao, D. Xiao, and X. Cui, Nat. Nanotechnol. **7**, 490 (2012).

[11] E. J. Sie, J. W. McIver, Y.-H. Lee, L. Fu, J. Kong, and N. Gedik, Nat. Mater. **14**, 290 (2015).

[12] K. F. Mak, K. L. McGill, J. Park, and P. L. McEuen, Science **344**, 1489 (2014).

[13] J. Lee, K. F. Mak, and J. Shan, Nat. Nanotechnol. **11**, 421 (2016).

[14] J. R. Schaibley, H. Yu, G. Clark, P. Rivera, J. S. Ross, K. L. Seyler, W. Yao, and X. Xu, Nat. Rev. Mater. **1**, 16055 (2016).

[15] F. Bussolotti, H. Kawai, Z. E. Ooi, V. Chellappan, D. Thian, A. L. C. Pang, and K. E. J. Goh, Nano Futures **2**, 032001 (2018).

[16] X. Xu, W. Yao, D. Xiao, and T. F. Heinz, Nat. Phys. **10**, 343 (2014).

[17] A. Ramasubramaniam and D. Naveh, Phys. Rev. B **87**, 195201 (2013).

[18] R. Mishra, W. Zhou, S. J. Pennycook, S. T. Pantelides, and J.-C. Idrobo, Phys. Rev. B **88**, 144409 (2013).

[19] H. Zheng, B. Yang, D. Wang, R. Han, X. Du, and Y. Yan, Appl. Phys. Lett. **104**, 132403 (2014).

[20] L. Cai, J. He, Q. Liu, T. Yao, L. Chen, W. Yan, F. Hu, Y. Jiang, Y. Zhao, T. Hu, Z. Sun, and S. Wei, J. Am. Chem. Soc. **137**, 2622 (2015).

[21] W.-Y. Tong, S.-J. Gong, X. Wan, and C.-G. Duan, Nat. Commun. **7**, 13612 (2016).

[22] J. Liu, W.-J. Hou, C. Cheng, H.-X. Fu, J.-T. Sun, and S. Meng, J. Phys.: Condens. Matter **29**, 255501 (2017).

[23] Y. Li, J. Ludwig, T. Low, A. Chernikov, X. Cui, G. Arefe, Y. D. Kim, A. M. van der Zande, A. Rigosi, H. M. Hill, S. H. Kim, J. Hone, Z. Li, D. Smirnov, and T. F. Heinz, Phys. Rev. Lett. **113**, 266804 (2014).

[24] A. V. Stier, K. M. McCreary, B. T. Jonker, J. Kono, and S. A. Crooker, Nat. Commun. **7**, 10643 (2016).

[25] J. Qi, X. Li, Q. Niu, and J. Feng, Phys. Rev. B **92**, 121403(R) (2015).

[26] Q. Zhang, S. A. Yang, W. Mi, Y. Cheng, and U. Schwingenschlögl, Adv. Mater. **28**, 959 (2016).

[27] X. Liang, L. Deng, F. Huang, T. Tang, C. Wang, Y. Zhu, J. Qin, Y. Zhang, B. Peng, and L. Bi, Nanoscale **9**, 9502 (2017).

[28] C. Zhao, T. Norden, P. Zhang, P. Zhao, Y. Cheng, F. Sun, J. P. Parry, P. Taheri, J. Wang, Y. Yang, T. Scrace, K. Kang, S. Yang, G. Miao, R. Sabirianov, G. Kioseoglou, W. Huang, A. Petrou, and H. Zeng, Nat. Nanotechnol. **12**, 757 (2017).

[29] I. Žutić, A. Matos-Abiague, B. Scharf, H. Dery, and K. Belashchenko, Mater. Today **22**, 85 (2019).

[30] B. Scharf, G. Xu, A. Matos-Abiague, and I. Žutić, Phys. Rev. Lett. **119**, 127403 (2017).

[31] P. Lazić, K. D. Belashchenko, and I. Žutić, Phys. Rev. B **93**, 241401(R) (2016).

[32] Z. Qiao, W. Ren, H. Chen, L. Bellaiche, Z. Zhang, A. H. MacDonald, and Q. Niu, Phys. Rev. Lett. **112**, 116404 (2014).

[33] P. Lazić, G. M. Sipahi, R. K. Kawakami, and I. Žutić, Phys. Rev. B **90**, 085429 (2014).

[34] C. Gong, L. Li, Z. Li, H. Ji, A. Stern, Y. Xia, T. Cao, W. Bao, C. Wang, Y. Wang, Z. Q. Qiu, R. J. Cava, S. G. Louie, J. Xia, and X. Zhang, Nature (London) **546**, 265 (2017).

[35] B. Huang, G. Clark, E. Navarro-Moratalla, D. R. Klein, R. Cheng, K. L. Seyler, D. Zhong, E. Schmidgall, M. A. McGuire, D. H. Cobden, W. Yao, D. Xiao, P. Jarillo-Herrero, and X. Xu, Nature (London) **546**, 270 (2017).

[36] A. K. Geim and I. V. Grigorieva, Nature (London) **499**, 419 (2013).

[37] K. S. Novoselov, A. Mishchenko, A. Carvalho, and A. H. C. Neto, Science **353**, aac9439 (2016).

[38] D. Zhong, K. L. Seyler, X. Linpeng, R. Cheng, N. Sivadas, B. Huang, E. Schmidgall, T. Taniguchi, K. Watanabe, M. A. McGuire, W. Yao, D. Xiao, K.-M. C. Fu, and X. Xu, Sci. Adv. **3**, e1603113 (2017).

[39] K. L. Seyler, D. Zhong, B. Huang, X. Linpeng, N. P. Wilson, T. Taniguchi, K. Watanabe, W. Yao, D. Xiao, M. A. McGuire, K.-M. C. Fu, and X. Xu, Nano Lett. **18**, 3823 (2018).

[40] P. E. Blöchl, Phys. Rev. B **50**, 17953 (1994).

[41] G. Kresse and D. Joubert, Phys. Rev. B **59**, 1758 (1999).

[42] G. Kresse and J. Furthmüller, Comput. Mater. Sci. **6**, 15 (1996).

[43] G. Kresse and J. Furthmüller, Phys. Rev. B **54**, 11169 (1996).

[44] J. P. Perdew, K. Burke, and M. Ernzerhof, Phys. Rev. Lett. **77**, 3865 (1996).

[45] J. Klimeš, D. R. Bowler, and A. Michaelides, J. Phys.: Condens. Matter **22**, 022201 (2010).

[46] J. Klimeš, D. R. Bowler, and A. Michaelides, Phys. Rev. B **83**, 195131 (2011).

[47] X. Wang, J. R. Yates, I. Souza, and D. Vanderbilt, Phys. Rev. B **74**, 195118 (2006).

[48] A. A. Mostofi, J. R. Yates, Y.-S. Lee, I. Souza, D. Vanderbilt, and N. Marzari, Comput. Phys. Commun. **178**, 685 (2008).

[49] M. A. McGuire, H. Dixit, V. R. Cooper, and B. C. Sales, Chem. Mater. **27**, 612 (2015).

[50] J. A. Wilson and A. D. Yoffe, Adv. Phys. **18**, 193 (1969).

[51] W.-B. Zhang, Q. Qu, P. Zhu, and C.-H. Lam, J. Mater. Chem. C **3**, 12457 (2015).

[52] Y. Ding, Y. Wang, J. Ni, L. Shi, S. Shi, and W. Tang, Phys. B: Condens. Matter **406**, 2254 (2011).

[53] J. Liu, Q. Sun, Y. Kawazoe, and P. Jena, Phys. Chem. Chem. Phys. **18**, 8777 (2016).

[54] T. Hu and J. Hong, ACS Appl. Mater. Interfaces **7**, 23489 (2015).

[55] J. E. Padilha, A. Fazzio, and A. J. R. da Silva, Phys. Rev. Lett. **114**, 066803 (2015).

[56] C. Jin, F. A. Rasmussen, and K. S. Thygesen, J. Phys. Chem. C **119**, 19928 (2015).

[57] S. D. Chakarova-Käck, E. Schröder, B. I. Lundqvist, and D. C. Langreth, Phys. Rev. Lett. **96**, 146107 (2006).

[58] G. Graziano, J. Klimeš, F. Fernandez-Alonso, and A. Michaelides, J. Phys.: Condens. Matter **24**, 424216 (2012).

[59] D. Xiao, G.-B. Liu, W. Feng, X. Xu, and W. Yao, Phys. Rev. Lett. **108**, 196802 (2012).

[60] V. O. Özçelik, J. G. Azadani, C. Yang, S. J. Koester, and T. Low, Phys. Rev. B **94**, 035125 (2016).

[61] D. MacNeill, C. Heikes, K. F. Mak, Z. Anderson, A. Kormányos, V. Zólyomi, J. Park, and D. C. Ralph, Phys. Rev. Lett. **114**, 037401 (2015).

[62] G. Aivazian, Z. Gong, A. M. Jones, R.-L. Chu, J. Yan, D. G. Mandrus, C. Zhang, D. Cobden, W. Yao, and X. Xu, Nat. Phys. **11**, 148 (2015).

[63] Z. Zhang, X. Ni, H. Huang, L. Hu, and F. Liu, Phys. Rev. B **99**, 115441 (2019).

[64] See Supplemental Material at http://link.aps.org/supplemental/10.1103/PhysRevB.101.125401 for details about the effect of heterostructure lattice constants, two-band tight-binding model Hamiltonian, hypothetic intralayer antiferromagnetic coupled CrI_3 monolayer, fitting parameters of the exponential function, and further calculation results and discussion.

[65] K. Zollner, P. E. Faria Junior, and J. Fabian, Phys. Rev. B **100**, 085128 (2019).

[66] H. Gao, W. Wu, T. Hu, A. Stroppa, X. Wang, B. Wang, F. Miao, and W. Ren, Sci. Rep. **8**, 7436 (2018).

[67] L. Xu, M. Yang, L. Shen, J. Zhou, T. Zhu, and Y. P. Feng, Phys. Rev. B **97**, 041405(R) (2018).